The structure and phase transformations in fumed transition alumina by X-ray diffraction and solid-state NMR

Jamal Nasir[1], Franz Schmidt[2], Frank Menzel[2], Jörn Schmedt auf der Günne[1]*

1 University of Siegen, Faculty IV: School of Science and Technology, Department of Chemistry and Biology, Inorganic Materials Chemistry and Center of Micro- and Nanochemistry and Engineering (Cµ), Adolf-Reichwein-Straße 2, D-57076 Siegen, Germany

2 Evonik, Operations GmbH, Rodenbacher Chaussee 4, D-63457 Hanau, Germany

*Email: gunnej@chemie.uni-siegen.de

Abstract

Powder X-ray diffraction, ^{27}Al solid-state NMR and TEM were used to study the structure and phase transformations in a series of transition alumina materials with BET surface areas ranging from 220 to 30 m^2/g produced by gas-to-particle flame method. During the short-lived synthesis, highly disordered γ-alumina progressively transforms into a mixture of δ and θ-alumina. For the well-crystallized mixture of δ and θ-alumina, high resolution and high S/N powder XRD pattern features a large number of superstructure reflections along with the commonly observed diffuse reflections. ^{27}Al MQMAS NMR provides a total of 8 crystallographic sites with an unusually high resolution in the tetrahedral region, with 4 distinct AlO_4 sites pertaining to the δ phase alone. We propose here based on data acquired on high-quality δ and θ-alumina that the bulk structures of both phases must be ordered.

**Keywords:** transition alumina, PXRD, solid-state NMR, MQMAS

Introduction

In catalytic activity, reactivity and properties, nano-scale alumina (Al_2O_3) particles made of "transition aluminas" play in a different league than those made of the most stable form the mineral corundum (α-Al_2O_3 or $R\bar{3}c$-Al_2O_3).[1–3] Vapor-phase synthesis of alumina nanoparticles have been extensively reviewed owing to the relevance of the materials in industry and basic science.[4,5] An important industrial process for their production is gas-phase combustion of $AlCl_3$ in the flame of an oxyhydrogen burner. $AlCl_3$, with a sublimation point of 180 °C, is vaporized in the flame and in an exothermic reaction converted into aluminium oxide at temperatures reaching up to about 2000 °C.[5]

$$2AlCl_3 + 3H_2 + 1.5O_2 \rightarrow Al_2O_3 + 6HCl \qquad (1)$$
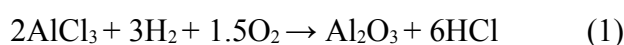
In a fast process, understood as a sequence of steps including nucleation, condensation and coalescence, aggregation and agglomeration (Figure 1), the Al_2O_3 particles are formed, which consist of small spherical particles joined into bigger objects of tree or chain-like structures. Aggregated nanostructured material based upon constituent particles in the range from 5 to 100 nm and with a BET surface area up to 350 m^2/g can be formed,[6] depending on the conditions of the cooling process in the gas phase. While the morphology of particles from this process is well studied,[7] insight into the atomic structure of the as-synthesized particles is rather limited[8] and only implies individual charges but not a systematic comparison, which is required to get an understanding of how the cooling process influences structural transitions. In general the surface areas increases with a faster cooling rate. Yet, the precise thermal history of the particles is difficult to determine experimentally.

The transition aluminas, which can be found under these conditions, generally have a much lower density of about 3.6 g/cm^3 than corundum with 3.98 g/cm^3.[9,10] Following Oswald's step rule, initially the most unstable phase is expected, which is γ-alumina, according to studies of other synthetic routes for the formation of transition alumina.[2,3,11] This phase is highly disordered on the Al site, while the O-atoms form a cubic closely packed arrangement and feature tetrahedrally and octahedrally coordinated Al atoms.[3,12] While in principle many transition aluminas have been reported,[2,3] relevant in the context of this contribution are only δ-/θ-alumina, which for example can be found upon thermal treatment of boehmite γ-AlOOH.[13,14]

$$\gamma\text{-AlOOH} \rightarrow \gamma \rightarrow \delta \rightarrow \theta \rightarrow \alpha\text{-}Al_2O_3 \quad (2)$$
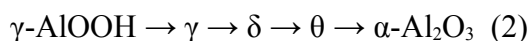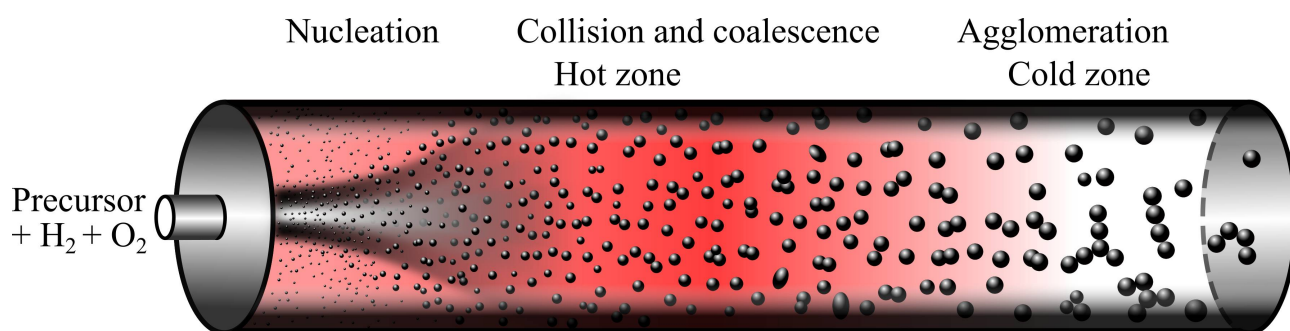
Figure 1: Processes occurring in the flame combustion synthesis of alumina in the flame of an oxyhydrogen burner.[4,5]

The structure of δ-alumina is still under discussion,[3,15,16] though a related structure, ω-alumina, could be described as an ordered structure with 9 Al sites in the orthorhombic system.[17] The structure solution of δ-alumina is complicated by intergrowth processes between different structures similar to ω-alumina. What is clear is that both the δ- and the related γ-alumina feature a cubic closed packed O sublattice and tetrahedrally (AlO_4) and octahedrally (AlO_6) coordinated Al atoms. [13,14,18] From the structure of ω-Al_2O_3, δ-alumina can be expected to have a ratio AlO_4/AlO_6 of approximately 3/5.[17] The next step in transformation is the formation to θ-alumina, which can be described as an ordered crystal structure in the monoclinic system with two Al sites one tetrahedrally and one octahedrally coordinated.[10,19]

A tool to study the uncertainty in the coordination number of the transition aluminas is solid-state nuclear magnetic resonance (NMR), which is inherently quantitative, element-selective and probes both crystalline and amorphous environments.[20–22] With respect to the different alumina polymorphs only recently a thorough review of the NMR literature has been published,[23] including computed and experimental values for isotropic chemical shift δ_{iso} and the quadrupole interaction. A particularly useful aspect of NMR is the unambiguous detection of the coordination number including pentacoordinated Al in context with the γ-alumina surface.[24–26]

The target of this contribution is to reach a better understanding of the transformation of transition aluminas produced in the combustion synthesis of alumina nano-particles from $AlCl_3$.

Experimental Part

Materials: All alumina samples were derived from $AlCl_3$ in hydrogen-air flame.

Synthesis of fumed alumina: $AlCl_3$ was used as the source of Al^{3+} ions, converted into gas phase and fed into oxyhydrogen flame as a homogeneous gas mixture with H_2, O_2, and the carrier gas. The vaporized $AlCl_3$ was transformed into fumed alumina through hydrolysis at high temperatures in the oxyhydrogen flame ($2H_2 + O_2 \rightarrow 2H_2O$) according to the already mentioned reaction.

Formed in flame residence times between 10 and 100 ms, the fumed alumina particles were in a mixed state with hot gases. The aerosol was then cooled before the solid particles were separated from the corrosive gas. In the final step, surface HCl was removed and high purity aluminium oxide was obtained.

Table 1: Some reaction conditions and sample properties of fumed alumina used in this study.

Label in manuscript	Theoretical BET surface area / (m^2/g)	Experimental BET surface area / (m^2/g)	Particle d (mean value) / nm	Evonik commercial label
BET 220	220	177*	5.4	Alu220 ex
BET 200	200	164*	5	Alu200 ex
BET 180	180	176	4	Alu180 ex
BET 130	130	115	7	Alu130
BET 100	100	101	8.6	AluC
BET 65	65	61	15	Alu65
BET 45	45	49	18	VP Alu45
BET 30	30	31	40	Alu30 ex

*The surfaces with BET over 200 may be unstable over a long period of time.

BET surface area: Triple-point Brunauer-Emmett-Teller (BET) measurements were conducted within the partial pressure region p/p_o of 0.05 to 0.3, in order to determine the specific surface area of alumina nanostructured particles. Prior to analysis, the samples were degassed for 20 min under vacuum at 150 °C. The BET analysis was carried out in accordance with DIN/ISO9277.

TEM: TEM images of fumed alumina were recorded via a field emission high-resolution transmission electron microscope Jeol 2010F (JEOL, Japan) using acceleration voltage of 200 kV.

The particles were dispersed in 50:50 v.% distilled water and isopropanol solution and afterwards dropped on a copper TEM grid following a drying step at room temperature for 30 min.

Solid-state NMR: ^{27}Al MAS NMR spectra were acquired at 156.393 MHz (14.1 T) on a 3.2 mm Bruker MAS probehead (Bruker Avance Neo NMR spectrometer) at 20 kHz spinning frequency. Unless otherwise specified in the results, a selective 90° pulse of 20 μs was applied with a repetition delay of 8 s, and 1024 scans were accumulated. The ^{1}H resonance of 1% TMS in $CDCl_3$ served as an external secondary reference using the Ξ values for [27]Al as reported by IUPAC.[27,28]

[27]Al multiple-quantum MAS (MQMAS) NMR spectra were also acquired at 156.393 MHz (14.1 T) on the 3.2 mm Bruker MAS probe head at 20 kHz spinning frequency. Three-pulse sequence [27]Al triple-quantum MQMAS[29] with a zero-quantum filter[30] and with rotor-synchronized sampling of the indirect dimension was utilized. Hard pulses of duration 4.5 and 1.5 μs for the excitation and conversion of quantum coherences, respectively, were determined by running an optimization experiment, and a 20 μs soft pulse (90°) was determined from [27]Al nutation experiments. Repetition delays were between 2 and 8 s depending on T_1 relaxation. Phase cycling involved the States method[31] for acquisition of pure absorption line shapes.

NMR spectral simulations were performed using DMfit software package (V 20230120).[32] Spectra for BET 220–100 were simulated using Czjzek model and for the BET 65–30 using the 'Q mas 1/2' model as implemented in Dmfit.[32,33]

Powder X-ray diffraction: Powder XRD measurements were carried out on a Huber Guinier powder camera G621 (Rimsting, Germany) in asymmetric transmission configuration. A curved Ge(111) monochromator was used to focus the incident beam and monochromatize it to select only Cu*Kα*₁ radiation.

Mylar foils (1 μm thick) were mounted on round metallic sample holders. Powder samples were placed on the Mylar foil and a second Mylar foil was placed on top of it (no grease was used to hold the powders tight). The powders trapped between the two foils were pressed to form flat round samples. The pressing was done in order to be able to measure a larger sample volume and increase signal-to-noise ratio as the materials are porous and have low crystallinity. Each round sample was measured repeatedly 16 or 64 times by rotating the sample holder in the plane of the sample step-wise, each time using an exposure time of 12 min. The diffraction images were recorded on a BaFX:Eu-based imaging plate (IP) film.[34] During the measurements, the samples were sliding side-ways in the X-ray beam. The X-ray exposed imaging plate was scanned using Typhoon FLA 7000

scanner (GE Company, USA). All the recorded diffraction images were digitized using the IPreader software and the averaging of 64 scans for BET30 and 16 scans for the rest of the samples was done by a gnuplot tcl-script.[34] Rietveld refinement[35] and other types of line shape analyses were performed using TOPAS-Academic V7 software package.[36]

Results and Discussion

The basis of this study is a series of alumina batches of materials from the combustion of $AlCl_3$ which underwent different thermal history. These batches feature different specific surface areas and structure. In the following, first the material morphology is studied by gas adsorption and electron microscopy. Then X-ray diffraction is applied to trace crystalline phases and finally solid-state NMR is applied to monitor the structural changes on an atomic scale.

Particle morphology: In total eight different batches of alumina nanoparticles were investigated which in the following will be named BET 30–BET 220 alumina according to their specific surface areas as measured by gas adsorption. "BET 220" stands for the batch from the fastest cooling process and has a theoretical specific surface area of 220 m^2/g (see Table 1 for the actual BET values).

The gas adsorption data (Table 1) show the expected scaling of the surface area A/m which for perfectly spherical nanoparticles should be inversely proportional to the particle diameter d and particle density ρ.

$$A/m = 6/(\rho \cdot d)$$

While the trend is well followed, deviations reflect both the changes in morphology and density because of the presence of different transition alumina (see below). The particle diameters as estimated from transmission electron microscopy are close to the expected values. Nevertheless, the material consists of aggregates and agglomerates and appears under ambient conditions as 'snow flakes' of mm to cm range. In water or other solvents high shear forces as e.g. by sonication, the aggregate structure can disrupt to smaller aggregates of down to d_{50} of 100 nm, forming stable dispersions.

Crystalline phase: Crystalline phases in BET 220–30 fumed aluminas were investigated by powder X-ray diffraction (Figure 2). Generally with increasing resident time in the flame during the synthesis the crystallinity increases, which is reflected by sharper reflection developing. On the way downwards on Oswald staircase towards α-Al_2O_3, several changes in crystal structure can be

observed including γ, δ, θ-alumina, each of which undergoes transformation into the subsequent phase from bottom to top as γ → (δ and θ) while the α-phase could not be observed. The observed sequence corresponds to the sequence observed for the crystallization of an alumina melt.[37]
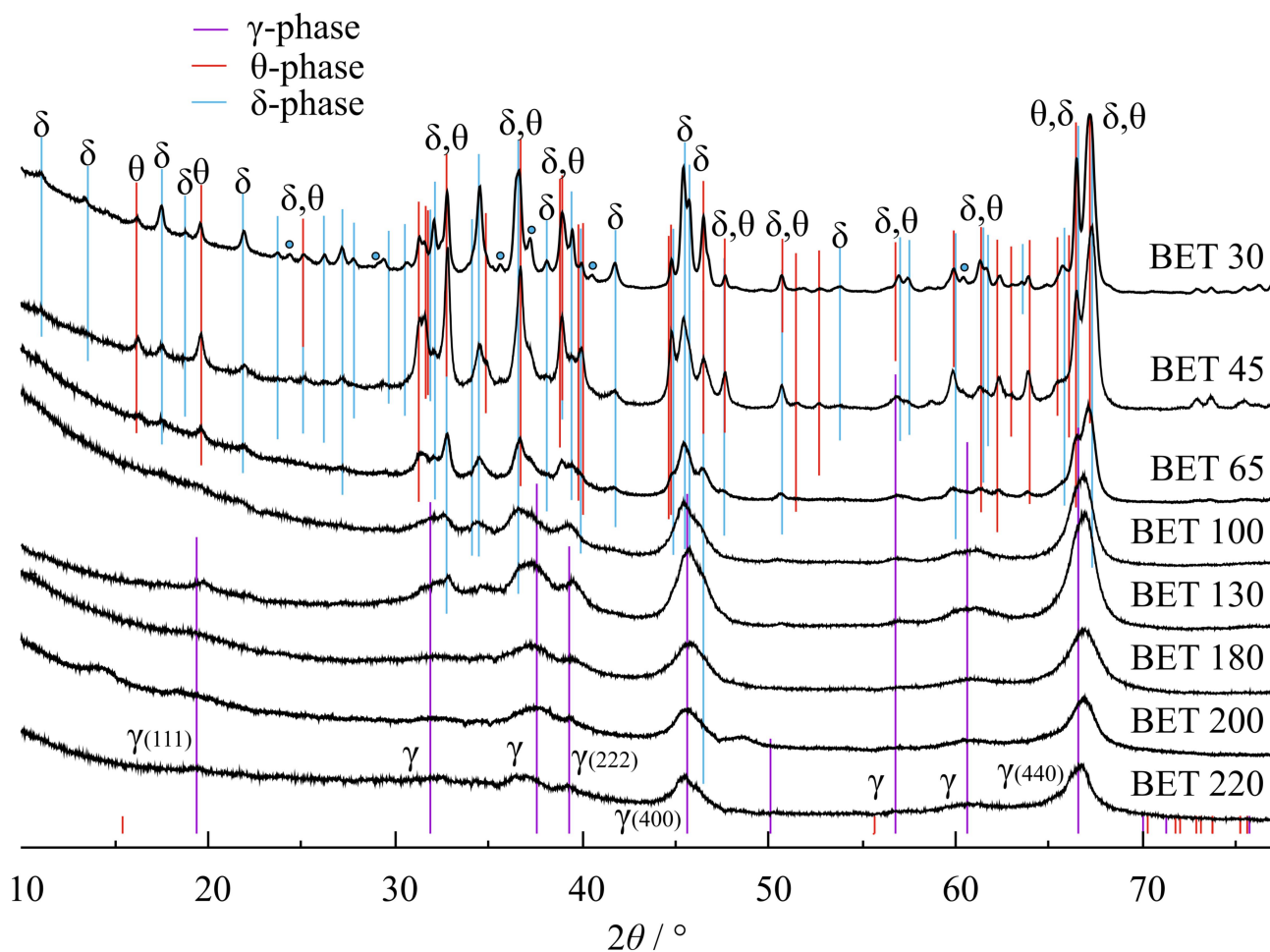

Figure 2: Powder XRD patterns of fumed alumina samples with BET 220–30. Three reference diffractograms γ-alumina ($Fd\bar{3}mZ$)[14], δ-alumina ($P222$)[45], and θ-alumina ($C12/m1$)[10] are shown as color coded vertical lines. The heights of the vertical lines do not correspond to the actual relative intensities but rather serve as visual guide, and some of the lines are deleted for the purpose of better visibility. The blue circles mark reflections non-existent in the δ model.

The observed diffraction patterns for the samples from BET 220–180 demonstrate only broad reflections with various line-widths. The composition of these samples are dominated by γ-alumina, which is evident by comparison to literature data.[38,39] The non-consistency in FWHM as a function

of 2θ has also been observed for boehmite-derived γ-alumina reflections and is to some degree obvious in Figure 2. However, the usually relatively sharp (222) reflection at 39.4°, is significantly broadened in the observed patterns and that is an indication of the small size of the crystallites.[40]

In the samples with even lower specific surface, i.e. BET 65 and below, δ-alumina is evident where the typical δ-triplet reflections between 44 and 47° take shape and the major reflection (400) at 66.7° overlapping with γ (440) occurs. Further decrease in BET leads to the appearance of a large number of superstructure δ reflections more in number than already observed in boehmite-derived δ-alumina.[15] The γ (440) reflection ultimately significantly splits into a very sharp θ-alumina and less sharper δ-alumina reflections indicating significant ordering of the θ phase. The BET 65 to 30 samples show that the transformations γ → δ and γ → θ are apparently occurring in parallel with the former being the faster (this observation is in agreement with the NMR data and is discussed also under NMR spectral simulations below).

The Rietveld refinement of the γ-phase in BET 220, 200 and 180 can be achieved using the spinel model with some non-spinel occupation of Smrcok et al. (Figure 3 and S1).[14] The Rietveld refinement, however, requires the occupancy of the non-spinel sites to be significantly higher than the boehmite-derived γ-alumina of Smrcok. While in Smrcok's refinement only 6.3% of all the non-spinel 16c and 48f sites are occupied by Al cations, in the fumed alumina the same type of occupancy reaches around 39%, 30% and 36% in BET 220, 200 and 180, respectively. The tetrahedral:octahedral relative occupation (64%:36%, 60%:40% and 64%:36%, respectively) remained relatively close to literature values of boehmite-derived γ-alumina. Fitting the occupancy of O (32e) gave values very close to 1 and did not affect the overall refinement. All the Al—O bond distances remained within 0.03% of those of Smrcok's model. While the overall fit looks convincing there is a clear disagreement with the tetrahedral:octahedral relative occupation (see below), which either indicates the presence of a significant amount of amorphous side-phase or a deficiency of the structural model.

The crystallite size obtained using integral breath approach by Rietveld refinement gave for the γ-alumina in the BET 220, 200 and 180 samples values of 8.2 ± 0.7, 8 ± 0.6 and 6 ± 0.2 nm, respectively. In comparison, the mean values for TEM-derived particle diameter for the same samples are 5.4, 5 and 4 nm, respectively. Given the non-monodisperse distribution of particle sizes, which have an impact on the analysis of the data from both TEM and XRD, this can be interpreted as a rough agreement meaning that crystallite and particle size are approximately the same (see Figure 8 and S5 for TEM images).
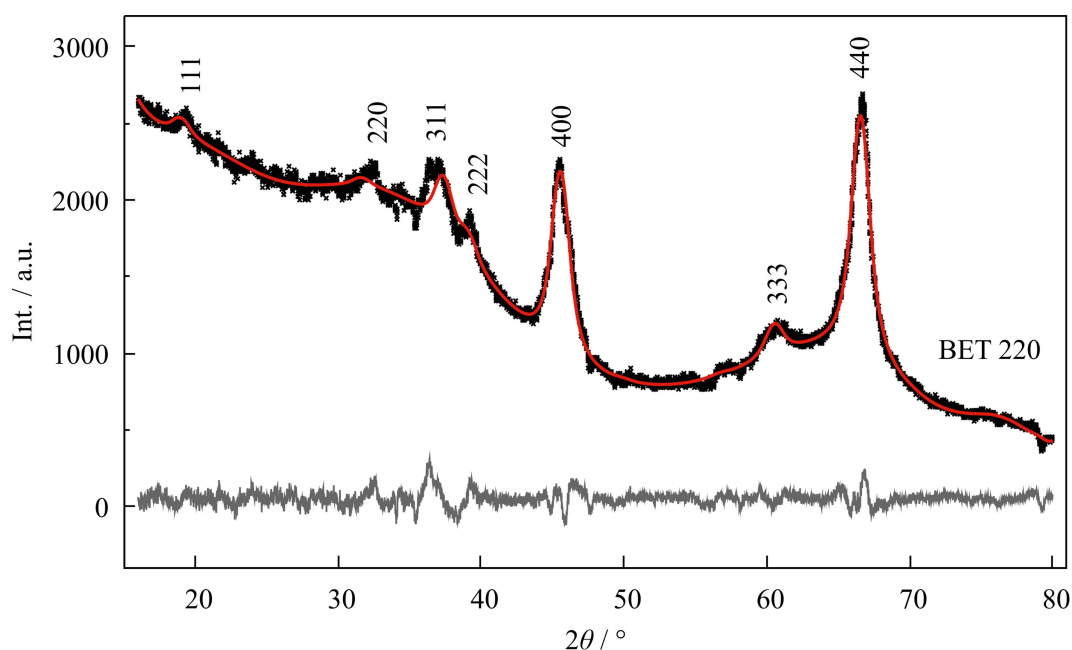
Figure 3: Rietveld refinement of BET 220 m^2/g sample using Smrcok et al. for γ alumina with a significant amount of non-spinel occupation. The black points represent the experimental data, the red solid line the calculated diffractogram with a residual profile factor of R_{wp} = 3.6%, and the grey line the difference. The input file is given in the SI in Table S1.

Local structure by ^{27}Al solid-state NMR: ^{27}Al MAS NMR provides information about the coordination number and frequency of the corresponding Al environment and for well crystallized materials information about the number of Al sites can be obtained besides.

The ^{27}Al MAS NMR spectra of (non-dehydrated) fumed alumina provide a consistent decrease in disorder and increase in crystallinity with increasing particle size (bottom to top, Figure 4), which is evident from the reduction of peak widths. This pattern across the samples agrees with the observations made from powder XRD. The samples with the highest specific surface area show a 2nd order quadrupolar broadened line-shape with a tail, typical of disordered phases, which gradually sharpen and transform into a typical 2nd order quadrupolar line-shape in ordered state.

The BET 220 sample, mainly consisting of γ phase, shows three Al coordination AlO_4, AlO_5 and AlO_6 with relative intensities of 30.1%, 21.5% and 48.4%, respectively (Figure S2). This observations is not agreeing with the results from the refinement of the powder X-ray pattern with Smrcok's model, which suggests that the tetrahedrally coordinated Al environment AlO_4 should be dominant. Furthermore a significant relative amount AlO_5 is observed.

9/21

Moving to the samples with lower specific surface area, the AlO_5 content drastically decreases to 8.6% at sample BET 200, less than 2% at sample BET 180, and to an unmeasurable amount beyond. The total intensities of AlO_4 and AlO_6 in Figure 4 do not change monotonically but roughly have plateau from BET 130 to 30 (see also Figure 7).

The ^{27}Al MAS measurements on the samples BET 220, 200, 180 and 130 kept under ambient conditions were repeated after 7 to 13 months with the same acquisition parameters, and the relative intensities and line-shapes remained almost the same (Figure S4). This indicates that the samples under ambient conditions are not subject to aging.

Two possible explanations for this observation are the presence of an amorphous side-phase besides the crystalline γ-alumina and the stabilization of AlO_5 at the surface of γ-alumina which may also explain the observed change in the ratio of tetrahedrally and octahedrally coordinated Al atoms. What can be ruled out is, that the surface alone is responsible for the stabilization of AlO_5 because the decay of the relative amount of AlO_5 is too fast (Figure 7) for the expected antiproportional scaling with the particle diameter.
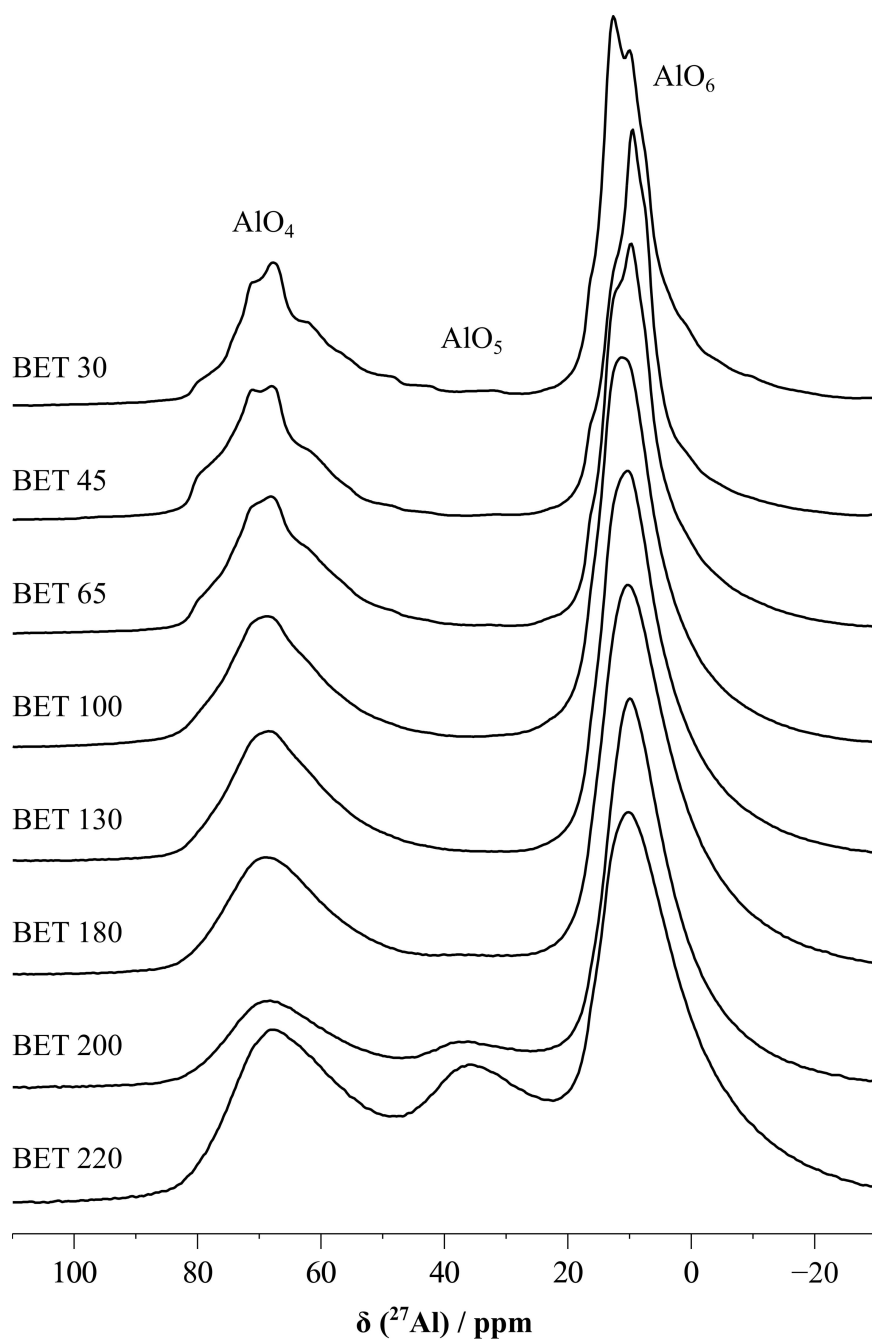
Figure 4: ^{27}Al MAS NMR spectra of fumed alumina with BET 220–30 measured at 20 kHz spinning frequency.

The AlO_4 and AlO_6 resonances in the spectra of the BET 30 and BET 45 samples in Figure 4 are a superposition of different resonances with a small chemical shift difference. Therefore, the MQMAS experiment was applied to achieve a better spectral resolution over the complete sample series.

For the samples from high to low specific surface area, the ^{27}Al MQMAS spectra of fumed alumina show a consistent line of narrowing and appearance of distinct resonances (Figure S3). The spectrum of the sample BET 220 shows three distinct sites – AlO_4, AlO_5 and AlO_6 – each of which has very broad distribution both in the direct and isotropic triple-quantum dimensions. The lack of line-narrowing in the isotropic dimension in the BET 220 and the next samples is evidence of large chemical shift distribution due to extensive disorder. From sample BET 130 and onward, the AlO_5 resonance disappears, and distinct peaks belonging to the sites of an ordered crystal structure can be resolved. From sample BET 100 and onward in the AlO_4 region of the spectrum three sites can be resolved. What these results indicate is that the samples are subject to a series of phase transitions which transform the complete grain.

For the samples with low specific surface area BET 45 and 30, MQMAS provided indeed a very high resolution which clearly evidences multiple distinct resonances (Figure 5 and S3). The MQMAS spectrum of sample BET 30 rendered an unusual high resolution of five distinct tetrahedral resonances alone. In the high-field corner of the same spectrum (Figure 5a), at least three AlO_6 resonances are recognizable in the isotropic dimension.

The pattern of phase transformations over all the samples can be clearly seen in the isotropic MQMAS projections which also shows a good agreement with the X-ray diffraction data, especially the changes in the tetrahedral region (Figure 6), which also reflect the high crystallinity of the compounds of low specific surface area.
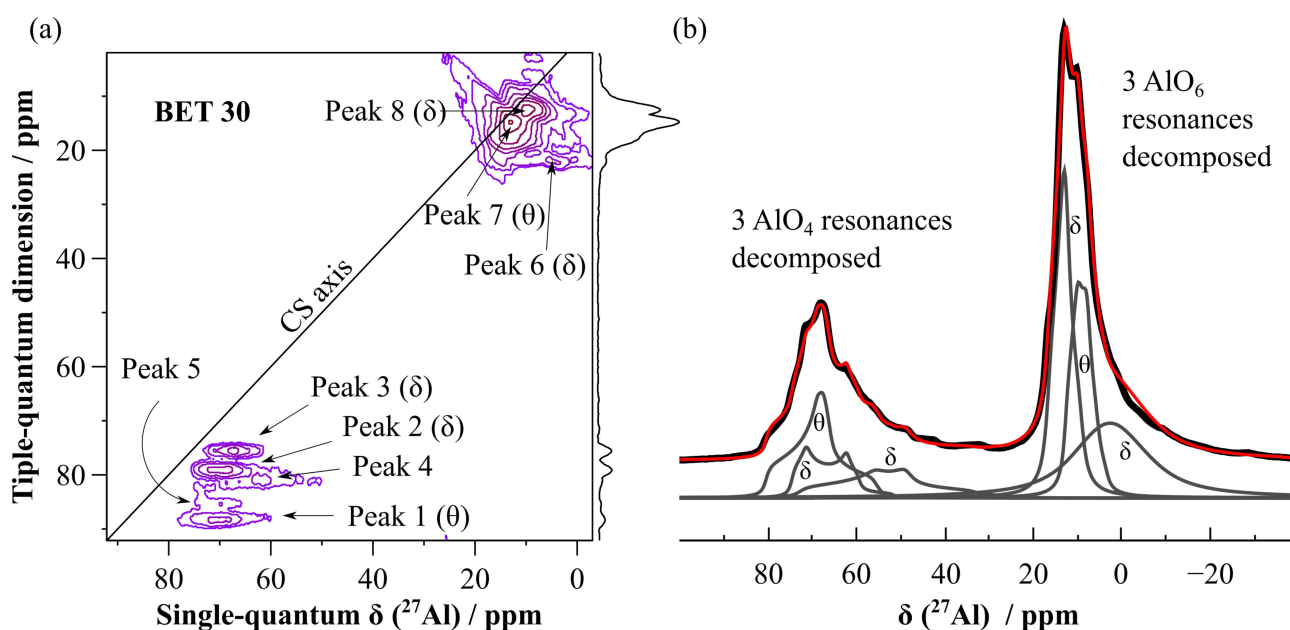
Figure 5: (a) Sheared ^{27}Al triple-quantum MQMAS NMR spectrum of fumed alumina with BET 30. (b) ^{27}Al MAS and simulated spectrum using quadrupolar central transition model. The measurements are carried out 20 kHz MAS frequency. In (b) the experimental data are shown in black, the total simulated spectra in red, and the individual decomposed spectra in grey. The assignments in the MQMAS spectra are done following the simulations of the 1D spectra.

Spectral simulations of ^{27}Al MAS data: In order to obtain a more quantitative description of the processes happening in the fumed alumina particles and the peaks which could be assigned to δ and θ alumina, the ^{27}Al NMR spectra were simulated. The MQMAS spectra and their projections on the isotropic dimension (Figure 6) qualitatively helped to simulate the ^{27}Al MAS spectra (the extracted spectral parameters are reported in Table 2, and for all the samples in Table S2). The MAS spectra of the highly disordered samples (BET 220 to 100) were simulated using the Czjzek model as implemented in the DMfit software,[41,42] and the chemical shift values for the AlO$_4$, AlO$_5$ and AlO$_6$ sites were determined at around 75, 42 and 15 ppm, respectively. For the samples with BET < 100 m^2/g, quadrupolar central transition model was used with which the two high-temperature transition aluminas, δ and θ, could be analysed. Despite the high resolution MQMAS spectra of BET 30 and 45 samples, two of the five AlO$_4$ resonances could not be fitted because of low signal to noise. Nevertheless a total of six resonances (3 × AlO$_4$ and 3 × AlO$_6$) were fitted to each of these spectra (Figure 5, S2, Table 2 and Table S2). In the series of measured ^{27}Al MQMAS spectra, the unprecedented resolution reached in BET 30 (Figure 5) shows that the crystallization has developed to the extent that both δ- and θ-alumina can be considered as ordered phases. The

AlO$_4$ signal region of sample BET 30 contains only well-resolved isotropic resonances both for δ-alumina (four distinct resonances) and θ-alumina (one distinct resonance) which means that both structures cannot be disordered.

The well-defined quadrupolar shape of the tetrahedral line in the θ phase[20] was useful in the fitting procedure and made the entire fit more reliable; a rough 1:1 ratio of AlO$_4$:AlO$_6$ integrated intensity was imposed. Integrating the models gave a higher θ-alumina content in the sample BET 45 (54%) than in the sample BET 30 (34%). Three types of measurements – XRD, MAS NMR and MQMAS – consistently show the highest θ intensity in BET 45 in all the samples. Therefore, two transformations, γ → δ and γ → θ, are apparently occuring in parallel.
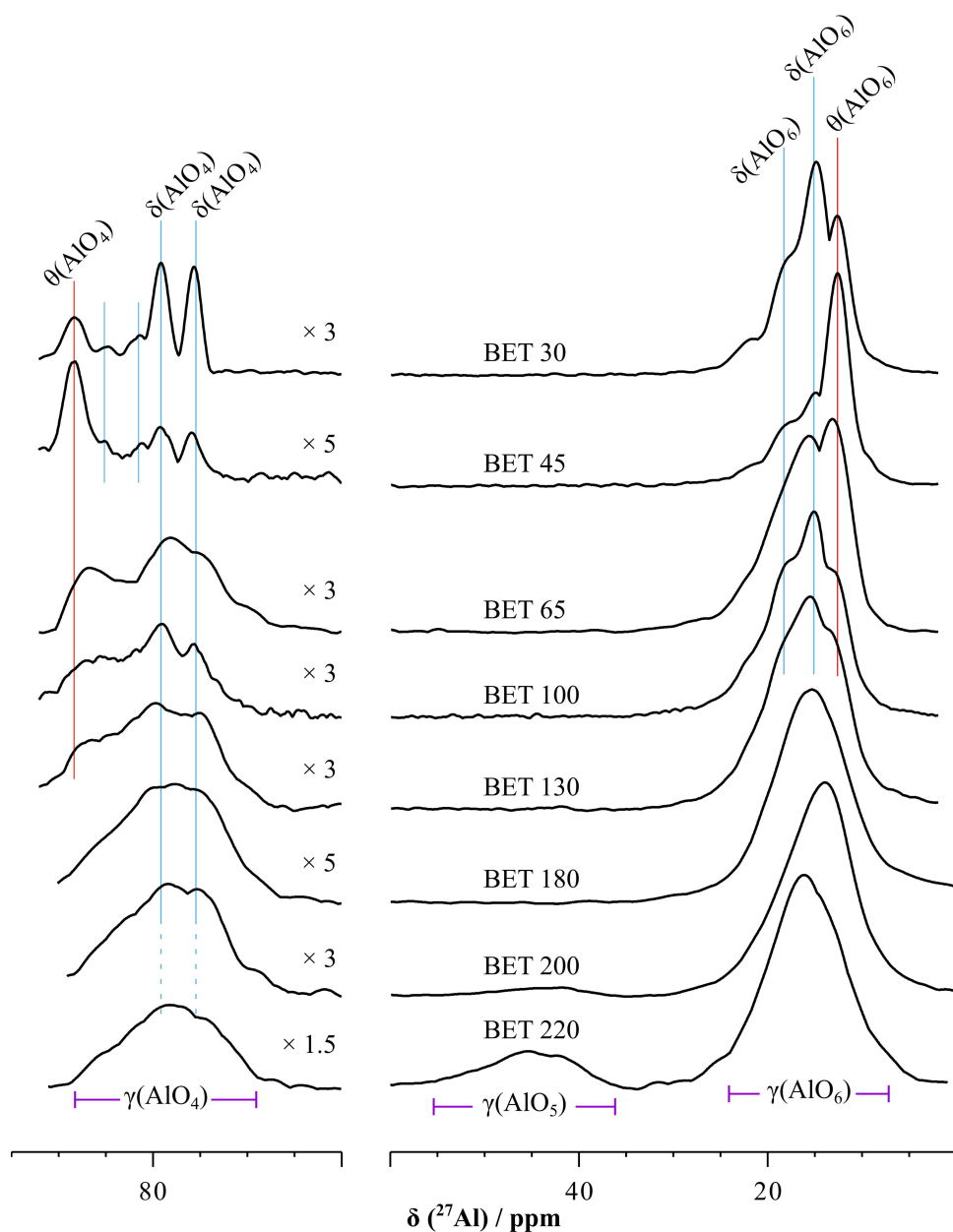
Figure 6: Sum projections of ^{27}Al triple-quantum MQMAS spectra of fumed alumina samples with BET 220–30 measured at 20 kHz MAS frequency. In the shearing execution, not all the 2D spectra are shifted by the same value.

Table 2: ^{27}Al MAS NMR parameters for the AlO$_4$, AlO$_5$ and AlO$_6$ sites in fumed alumina materials obtained by using DMfit package and the corresponding literature values (complete table for all the samples are given in Table S2.

BET / m²/g	Main phase	Type	δ_{iso} / ppm	C_Q / MHz	η	Model used	Relative intensities	Comment
	γ-Al$_2$O$_3$	AlO$_4$	77.5 ± 0.2	3.5 ± 0.1		Czjzek	10%	[43]
		AlO$_5$	37.2 ± 0.2	4.5 ± 0.1			13%	
		AlO$_6$	14.0 ± 0.2	4.3 ± 0.1			78%	DNP NMR
	δ-alumina	AlO$_4$	73.2	4.6	0.6		19.6%	[44] Al isopropoxide precursor; sol-gel
		AlO$_4$	68.3	6.6	0.4		20.7%	
		AlO$_6$	16.3	4.8	0.0		25.8%	
		AlO$_6$	14.5	4.3	0.6		33.9%	
	θ-alumina	AlO$_4$	80 (1)	6.4 (0.1)	0.65(0.02)		47.8%	[20] Al tributoxide precursor; sol-gel
		AlO$_6$	10.5 (1)	3.5 (0.3)	0(0.1)		52.2%	
BET 220	γ-alumina	AlO$_4$	75	6.6		Czjzek	30.1%	This study
		AlO$_5$	42	6.2			21.5%	
		AlO$_6$	15.3	5.6			48.4%	
BET 30	θ-alumina	AlO$_4$	80.4	6.1	0.9	Q mas 1/2	15.6%	This study
		AlO$_6$	12.7	3.9	0.5		18.3%	
	δ-alumina	AlO$_4$	76.6	6.4	0.2		8%	
		AlO$_4$	73.3	8.3	0.7		9%	
		AlO$_6$	16.4	3.3	1		24.1%	
		AlO$_6$	10.2	5.2	0.7		25%	

De-/rehydration experiments and structural model: To get a better understanding of the sample surface the samples were exposed to vacuum at 295 K, which leads to a partial dehydration of the sample surface. The sample BET 220 was slowly rehydrated by contact with air and the process monitored by ^{27}Al NMR. The measurements show that around 10% of AlO_6 and AlO_5 interconverts (Figure 7b); a significant interconversion between AlO_5 and AlO_6, however, is not evident in the MAS measurements. Because re-/dehydration is expected at the surface, it can be concluded that water molecules coordinate the aluminium atoms and upon dehydration cause a change of the coordination number. Note that the condensation of two Al-O-H groups would not cause a change of the coordination number as observed. Because AlO_5 (Figure 7b) is not completely converted into AlO_6 by rehydration indicates that a significant amount of AlO_5 is not directly at the particle surface.
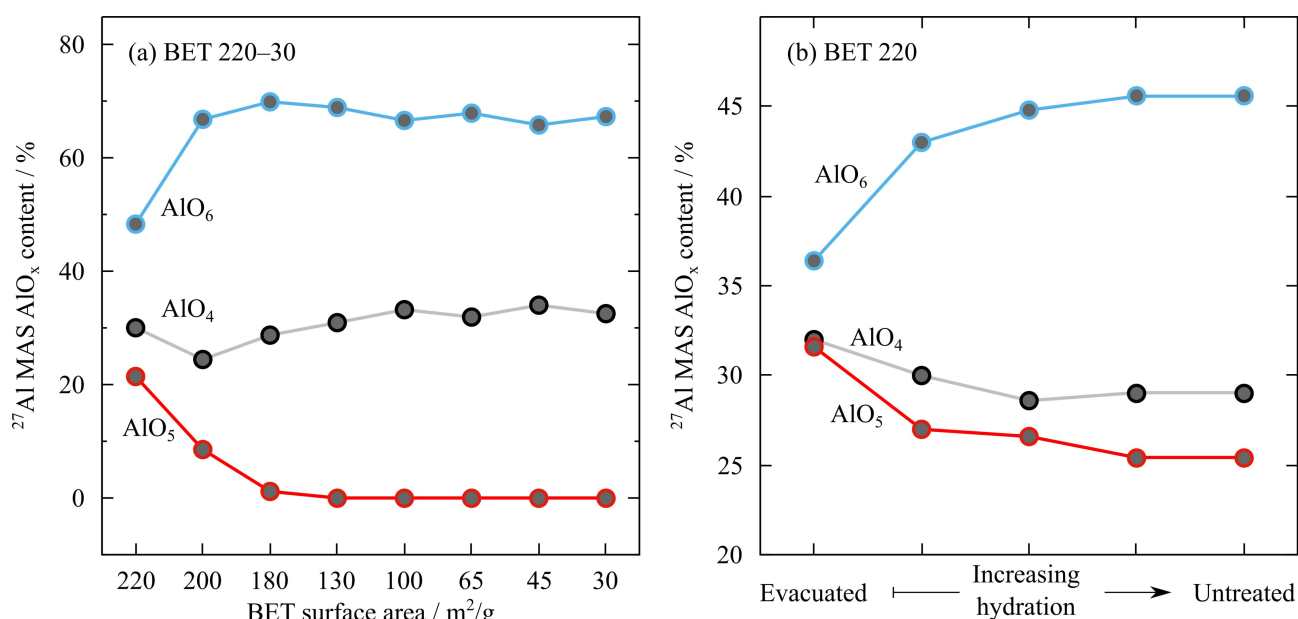

Figure 7: (a) AlO_4, AlO_5 and AlO_6 contents in BET 220-30 fumed alumina samples measured by ^{27}Al MAS NMR and (b) after low-vacuum evacuation at 300 °C for 2 days of the sample and rehydroxylation/rehydration of the samples step-by-step inside the rotor after each measurement. The spectra were acquired using a 30° tip angle at 100 kHz nutation frequency.
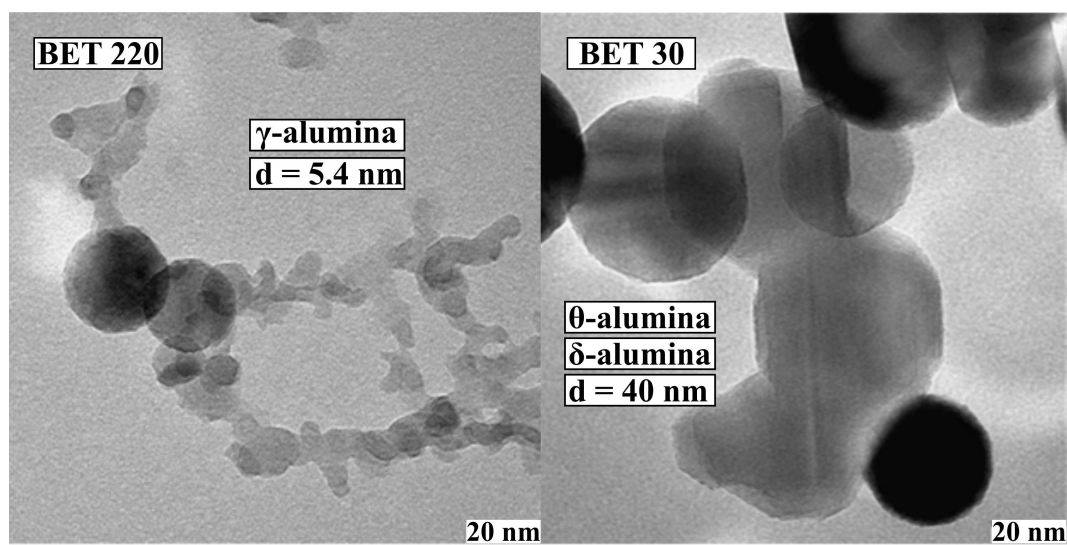
Figure 8: TEM images of BET 220 (left) and BET 30 (right) fumed alumina samples. The BET 220 sample, mainly γ-alumina, undergoes a transformation pathway as γ → δ,θ leading to well-crystalline δ and θ-alumina in BET 30.

Conclusions

It was shown that the crystallization of alumina starting with a nucleation in the gas phase passes through the sequence of γ, δ and θ metastable phases. The γ → δ ordering starts earlier and proceeds faster than the γ → θ transformation which leads to both the δ and θ becoming ordered phases in the well-crystallized BET 30 sample. Although powder XRD data showed relatively sharp reflections, it was mainly ^{27}Al MQMAS NMR that provided evidence for the ordered nature of both δ and θ giving an impressive four distinct peaks for the tetrahedral sites in δ alone. Moreover, evacuation of fumed alumina, rehydration and ^{27}Al MAS NMR measurements showed that AlO_5 is only partially present at the surface; in the case of BET 220 fumed alumina (mainly γ phase), around 10% of AlO_6 was transformed into AlO_5 and AlO_4.

CRediT author statement:

Formal analysis: JN; Investigation: JN, FS, FM; Writing - Original Draft: JN; Visualization: JN, FM, FS; Project administration: JSADG; Conceptualization: JSADG; Writing - Review & Editing: JSADG; Supervision: JSDAG.

References

[1] H. Pines, W.O. Haag, J. Am. Chem. Soc. 82 (1960) 2471–2483.

[2] K. Wefers, C. Misra, (1987).

[3] I. Levin, D. Brandon, J. Am. Ceram. Soc. 81 (2005) 1995–2012.

[4] S.E. Pratsinis, S. Vemury, Powder Technol. 88 (1996) 267–273.

[5] M.S. Wooldridge, Prog. Energy Combust. Sci. 24 (1998) 63–87.

[6] V.M. Gun'ko, Y.M. Nychiporuk, V.I. Zarko, E.V. Goncharuk, O.A. Mishchuk, R. Leboda, J. Skubiszewska-Zięba, E. Skwarek, W. Janusz, G.R. Yurchenko, V.D. Osovskii, Y.G. Ptushinskii, V.V. Turov, P.P. Gorbik, J.P. Blitz, K. Gude, Appl. Surf. Sci. 253 (2007) 3215–3230.

[7] V.M. Gun'ko, V.I. Zarko, O.V. Goncharuk, A.K. Matkovsky, O.S. Remez, J. Skubiszewska-Zięba, G. Wojcik, B. Walusiak, J.P. Blitz, Appl. Surf. Sci. 366 (2016) 410–423.

[8] P. Kaur, A. Khanna, N. Kaur, P. Nayar, B. Chen, Phase Transitions 93 (2020) 596–605.

[9] J. Lewis, D. Schwarzenbach, H.D. Flack, Acta Cryst. A 38 (1982) 733–739.

[10] E. Husson, Y. Repelin, Eur. J. Solid State Inorg. Chem. 33 (1996) 1223–1231.

[11] X. Krokidis, P. Raybaud, A.-E. Gobichon, B. Rebours, P. Euzen, H. Toulhoat, J. Phys. Chem. B 105 (2001) 5121–5130.

[12] A. Boumaza, L. Favaro, J. Lédion, G. Sattonnay, J.B. Brubach, P. Berthet, A.M. Huntz, P. Roy, R. Tétot, Journal of Solid State Chemistry 182 (2009) 1171–1176.

[13] R.S. Zhou, R.L. Snyder, Acta Crystallographica Section B Structural Science 47 (1991) 617–630.

[14] Ľ. Smrčok, V. Langer, J. Křesťan, Acta Crystallogr., Sect. C: Cryst. Struct. Commun. 62 (2006) i83–i84.

[15] S.V. Tsybulya, G.N. Kryukova, Powder Diffr. 18 (2003) 309–311.

[16] L. Kovarik, M. Bowden, D. Shi, J. Szanyi, C.H.F. Peden, J. Phys. Chem. C 123 (2019) 9454–9460.

[17] G. Wallez, J. Solid State Chem. 312 (2022) 123303.

[18] L. Kovarik, M. Bowden, A. Genc, J. Szanyi, C.H.F. Peden, J.H. Kwak, J. Phys. Chem. C 118 (2014) 18051–18058.

[19] G. Yamaguchi, I. Yasui, W.-C. Chiu, Bull. Chem. Soc. Jpn. 43 (1970) 2487–2491.

[20] L.A. O'Dell, S.L.P. Savin, A.V. Chadwick, M.E. Smith, Solid State Nucl. Magn. Reson. 31 (2007) 169–173.

[21] J.Z. Hu, S. Xu, J.H. Kwak, M.Y. Hu, C. Wan, Z. Zhao, J. Szanyi, X. Bao, X. Han, Y. Wang, C.H.F. Peden, J. Catal. 336 (2016) 85–93.

[22] S. Xu, N.R. Jaegers, W. Hu, J.H. Kwak, X. Bao, J. Sun, Y. Wang, J.Z. Hu, ACS Omega 6 (2021) 4090–4099.

[23] C.V. Chandran, C.E.A. Kirschhock, S. Radhakrishnan, F. Taulelle, J.A. Martens, E. Breynaert, Chem. Soc. Rev. 48 (2019) 134–156.

[24] J.Z. Hu, S. Xu, J.H. Kwak, M.Y. Hu, C. Wan, Z. Zhao, J. Szanyi, X. Bao, X. Han, Y. Wang, C.H.F. Peden, Journal of Catalysis 336 (2016) 85–93.

[25] J.H. Kwak, J. Hu, D. Mei, C.-W. Yi, D.H. Kim, C.H.F. Peden, L.F. Allard, J. Szanyi, Science 325 (2009) 1670–1673.

[26] H.-I. Kim, S.K. Lee, American Mineralogist 106 (2021) 389–403.

[27] R.K. Harris, E.D. Becker, Journal of Magnetic Resonance 156 (2002) 323–326.

[28] R.K. Harris, E.D. Becker, S.M. Cabral de Menezes, P. Granger, R.E. Hoffman, K.W. Zilm, Pure Appl. Chem. 80 (2008) 59–84.

[29] L. Frydman, J.S. Harwood, J. Am. Chem. Soc. 117 (1995) 5367–5368.

[30] J.-P. Amoureux, C. Fernandez, S. Steuernagel, J. Magn. Reson., Ser. A 123 (1996) 116–118.

[31] D.J. States, R.A. Haberkorn, D.J. Ruben, J. Magn. Reson. (1969) 48 (1982) 286–292.

[32]   D. Massiot, F. Fayon, M. Capron, I. King, S. Le Calvé, B. Alonso, J.-O. Durand, B. Bujoli, Z. Gan, G. Hoatson, Magn. Reson. Chem. 40 (2002) 70–76.

[33]   G. Czjzek, J. Fink, F. Götz, H. Schmidt, J.M.D. Coey, J.-P. Rebouillat, A. Liénard, Phys. Rev. B 23 (1981) 2513–2530.

[34]   J. Nasir, N. Steinbrück, K. Xu, B. Engelen, J. Schmedt Auf Der Günne, J. Appl. Crystallogr. 55 (2022) 1097–1103.

[35]   H.M. Rietveld, J. Appl. Cryst. 2 (1969) 65–71.

[36]   A.A. Coelho, J. Appl. Cryst. 51 (2018) 210–218.

[37]   V. Jayaram, C.G. Levi, Acta Metall. 37 (1989) 569–578.

[38]   B.C. Lippens, J.H. de Boer, Acta Cryst 17 (1964) 1312–1321.

[39]   R.-S. Zhou, R.L. Snyder, Acta Crystallogr B Struct Sci 47 (1991) 617–630.

[40]   S.V. Tsybulya, G.N. Kryukova, Phys. Rev. B 77 (2008) 024112.

[41]   D. Massiot, F. Fayon, M. Capron, I. King, S. Le Calvé, B. Alonso, J.-O. Durand, B. Bujoli, Z. Gan, G. Hoatson, Magn. Reson. Chem. 40 (2002) 70–76.

[42]   G. Czjzek, J. Fink, F. Götz, H. Schmidt, J.M.D. Coey, J.-P. Rebouillat, A. Liénard, Phys. Rev. B 23 (1981) 2513–2530.

[43]   M. Mais, S. Paul, N.S. Barrow, J.J. Titman, Johnson Matthey Technol. Rev. 62 (2018) 271–278.

[44]   S. Xu, N.R. Jaegers, W. Hu, J.H. Kwak, X. Bao, J. Sun, Y. Wang, J.Z. Hu, ACS Omega 6 (2021) 4090–4099.

[45]   D. Fargeot, D. Mercurio, A. Dauger, Mate. Chem. Phys. 24 (1990) 299–314.